Geophysical Research Letters

RESEARCH LETTER
10.1029/2018GL077388

Special Section:
New understanding of the solar eclipse effects on geospace: The 21 August 2017 Solar Eclipse

Atmospheric Gravity Waves in the Ionosphere and Thermosphere During the 2017 Solar Eclipse

Cissi Y. Lin[1], Yue Deng[1], and Aaron Ridley[2]

[1]Department of Physics, University of Texas at Arlington, Arlington, TX, USA, [2]Department of Atmospheric, Oceanic, and Space Sciences, University of Michigan, Ann Arbor, MI, USA

Key Points:
- Supersonically moving lunar shadow induces mesoscale waves at totality locations
- A bow wave front led by the lunar shadow is formed with modification of the in situ forcing
- VTEC have strong wave responses with periods of 20-30 min

Correspondence to:
Y. Deng,
yuedeng@uta.edu

Citation:
Lin, C. Y., Deng, Y., & Ridley, A. (2018). Atmospheric gravity waves in the ionosphere and thermosphere during the 2017 solar eclipse. *Geophysical Research Letters*, *45*, 5246–5252. https://doi.org/10.1029/2018GL077388

Received 31 JAN 2018
Accepted 6 APR 2018
Accepted article online 19 APR 2018
Published online 5 JUN 2018

Abstract As a cavity of solar radiation created by the lunar shadow moves across the United States on 21 August 2017, decreases in local ionospheric and thermospheric (IT) temperature and density are anticipated. The average velocity of the total solar eclipse across the United States is ~700 m/s. The supersonically moving lunar shadow has induced bow waves and gravity waves that are observed by the Global Navigation Satellite System (GNSS) network. We use the Global Ionosphere-Thermosphere Model, a global circulation model solving for nonhydrostatic equations, with high-resolution (2° in longitude and 0.5° in latitude) and high-cadence (forcing updated every 2 s) settings to investigate the IT responses related to the atmospheric gravity wave perturbations during the solar eclipse. The modeled IT conditions extracted at 5-s cadence at two ground stations reveal different responses in both neutral and electron densities under totality and partial-eclipse scenarios. A bow wave of −0.2 TECu develops and lasts hours since totality, which is comparable with the GNSS observations. Gravity waves with period of 20–30 min observed by GNSS have been reproduced in our simulations.

Plain Language Summary Just as a boat moving through the surface of a lake stirs up waves in its wake, the lunar shadow moving across continents stirs up waves in our atmosphere during a solar eclipse. While the 2017 solar eclipse allowed a once-in-a-lifetime viewing opportunity for over 200 million Americans, it also allowed scientists to capture unambiguous bow waves predicted by theoretical studies decades ago with the modern Global Navigation Satellite System. In this study, we use a self-consistent global circulation model for the upper atmosphere to further confirm the formation of bow waves by the supersonically moving lunar shadow. Waves with period of 20–30 min observed by Global Navigation Satellite System have been reproduced in our simulations.

1. Introduction

The atmospheric response during a solar eclipse has been observed (Altadill et al., 2001; Jakowski et al., 2008; MacPherson et al., 2000) and studied for decades (Chimonas, 1970; Chimonas & Hines, 1971; Fritts & Luo, 1993). The path of the 2017 solar eclipse crossed 14 U.S. states, entering Oregon and leaving South Carolina, on 21 August 2017. The long duration of its totality path on land (~2 hr) provided a unique opportunity for scientific exploration in the modern age. Thousands of Global Navigation Satellite System (GNSS) receivers across the continental United States observed the event (Coster et al., 2017; Zhang et al., 2017). A wide community of ham radio operators participated in innovational experiments, HamSCI, to communicate using high-frequency radios (1–30 MHz) during the day. The Super Dual Auroral Radar Network and scintillation receivers were coordinated to observe the event simultaneously.

Total electron content (TEC) derived from GNSS receivers have captured large-scale and medium-scale traveling disturbances induced from various lower-atmospheric sources, including tsunamis (Galvan et al., 2011; Occhipinti et al., 2006; Saito et al., 2011; Tsugawa et al., 2011) and strong tropical systems in the troposphere (Nishioka et al., 2013; Perwitasari et al., 2015; Yue et al., 2014). Theoretical works have used moving wave packets as forcing to drive lower and upper atmospheric models (Hickey et al., 2009; Lin et al., 2017; Meng et al., 2015; Vadas et al., 2015). Depending on the propagation velocity, moving wave packets in the lower thermosphere induce acoustic or gravity waves. Upward propagating gravity waves result in perturbations observable in both neutral and electron densities. The induced perturbations in TEC may sustain tens of minutes to hours as gravity waves after the lower boundary wave packet has passed. The effects of

acoustic waves, however, are more transient and localized to the atmosphere encountering the wave packet than the effects of induced gravity waves (Lin et al., 2017).

Gravity waves observed in the upper atmosphere are primarily induced by (1) waves propagating from the lower atmosphere and (2) in situ modification to energy, chemistry, or dynamics. The reduction of heating sources (e.g., ozone at 45 km or extreme ultraviolet, EUV, heating above 100 km) in the atmosphere can become a source for generating atmospheric perturbations. Theoretical calculation (Chimonas, 1970; Chimonas & Hines, 1971; Fritts & Luo, 1993) has shown that such a source moving at supersonic speeds is expected to induce a bow wave and acoustic gravity waves in the lower atmosphere and may be observed in the form of traveling disturbances in the upper atmosphere. Global 3-D simulations have been performed to study the effects of a solar eclipse on the terrestrial atmosphere up to the altitude of ~80 km (Eckermann et al., 2007). In the study, the reduced ozone heating resulted in a distinguishable bow wave observed in geopotential height at a pressure of 0.01 hPa approximately 4 hr after the eclipse started. Owing to the limit of the model employed, the heating and cooling parameterization was not valid above 0.01 hPa. The results from a coarse-resolution global simulation of the upper atmosphere suggested that a solar eclipse may drive large-scale (greater than 1,000 km) wave-like features in temperature and neutral wind changes (Müller-Wodarg et al., 1998). The lunar shadow moved supersonically on 21 August 2017: averaging roughly 700 m/s (Huba & Drob, 2017), or about 1,000 m/s in Oregon and slowing to about 650 m/s in South Carolina (Coster et al., 2017). For the first time, the dense GNSS network provided measurements a unambiguous bow waves during the 21 August eclipse (Zhang et al., 2017). Mesoscale wave structures with a period of 25 min were observed, which agree with the prediction of a dominant wave period of ~20 min at an altitude of 300 km (Chimonas & Hines, 1971). In this study, the mesoscale features that may have been induced by the 2017 eclipse are presented. The Global Ionosphere-Thermosphere Model (GITM) is used to study aspects of the effect of the eclipse on the upper atmosphere that have not been studied previously.

2. Methodology

GITM is a self-consistent 3-D ionosphere-thermosphere model (Ridley et al., 2006) with the advantages of flexible 3-D grid sizes and the ability to solve for nonhydrostatic solutions (Deng et al., 2008; Deng & Ridley, 2014). For this study, we performed global simulations with the resolution of 2° by 0.5° in latitude and longitude, which is roughly equivalent to a resolution of 150 km by 50 km at the U.S. sector. The resolvable horizontal wavelength in the diagonal direction is 316 km. The altitudinal range extended from 100 to ~700 km with a vertical resolution of roughly one third of the scale height. The time step was roughly 2 s, which was needed in order to capture both the acoustic waves and normally strong ion flows at high latitudes. The simulations started at 13:30 UT on 20 August 2017 and ended at 23:30 UT on 21 August 2017. The first 24 hr was used to spin up the codes.

While the visible light is completely blocked by the lunar body during totality, the EUV radiation from the corona does not reduce completely, resulting in weakened but nonzero ionization and heating in the upper atmosphere. Marriott et al. (1971) considered the ratio of electron production rate during an eclipse to that on a regular day as the *obscuration factor*. Adopting the idea, Huba and Drob (2017) used solar images to predict the obscuration factor during the 2017 eclipse and applied the factor to the amount of EUV flux within the radius of the eclipsed atmosphere by the lunar shadow. In this study, the scaling factor is considered as 10% at totality, linearly increasing toward the edge of the impacted area at a radius of approximately 3,000 km and returning to 100% outside of the linear region with a smooth transition of a quarter sinusoidal function. Without considering the actual features on the solar disk, it implies a uniform EUV flux distribution and this factor is simply a function of radius of the shadow. The left panel of Figure 1 illustrates the temporal variation of the scaling factor for totality (blue) and partial-eclipse (orange) scenarios. This implementation allows effective calculation at each 2-s time step in the GITM simulation and facilitate the establishment a baseline for investigating high-frequency mesoscale perturbations caused by the eclipse.

Two separate simulations are performed: a control run and an eclipse run with the temporally and spatially varying scaling factor. The differences between the control run and the eclipse run are considered as consequential atmospheric responses to the eclipse. Particularly, thermospheric and ionospheric variables at two ground stations are extracted from the 3-D simulation. The stations are located in Missouri (MO, 39°N, 93°W) and Massachusetts (MA, 42.6°N, 71.5°W), where GNSS TEC or incoherent scatter radar

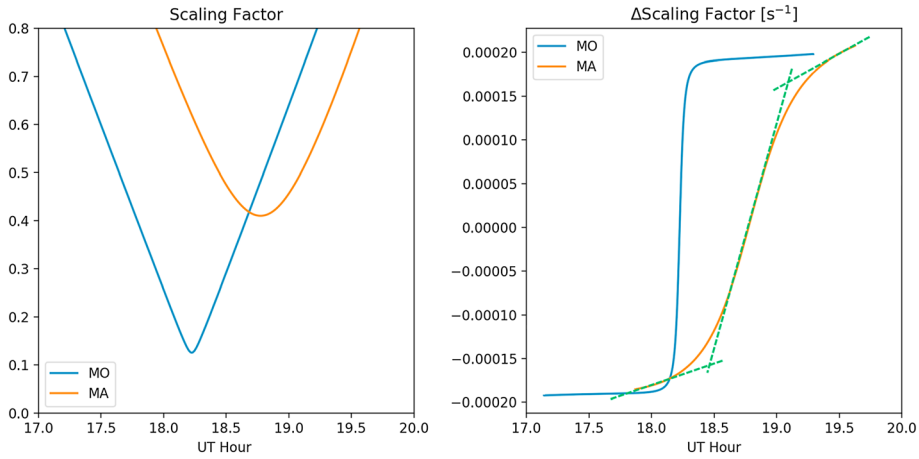

Figure 1. (left) Temporal variation of the extreme ultraviolet scaling factor at the MO and MA stations. (right) Change rate of the scaling factor at the two stations. The green dashed lines illustrate the estimation of the transition, defined by the linear approximation of the piecewise change rates.

measurements were taken. The MO station experienced totality, while the maximal obscuration at the MA station was 63%. The time for maximal obscuration at the two stations was 18:13 UT (13:13 CDT) and 18:46 UT (14:46 EDT), respectively.

3. Results

One-dimensional column values were extracted from the global 3-D simulation results at the two locations from about 3 hr before and 2 hr after totality. Figure 2 shows the differential fields of neutral mass density (left column) and electron number density (right column) at the two ground stations: (top) MO and (bottom) MA. The large-scale ionospheric and thermospheric responses at the two stations were similar but different in several fashions. The electron density showed similar trends at both stations. The maximal decrease below ~200 km occurs during maximal obscuration, marked by the black vertical line. The loss of solar EUV radiation resulted in a rapid decrease in the electron density in the *E* region as it is the main ionization source there. Transport contributes significantly to the electron density balance at the higher altitudes, where the maximal decrease occurs about 30 min later. The temperature decrease in the lower thermosphere, resulting from reduced EUV heating, peaked at 200 km and reached its minima of −41 and −42 K, at the MO and MA stations, respectively, ~30 min after maximal obscuration (not shown). Consequentially, the neutral density decreased by 25% at both stations. Wave activity in both mass density and electron density is clearly observable at the MO station as shown in Figures 2a and 2b. High-frequency waves are induced when local obscuration started and became more significant after the totality epoch as indicated by the vertical black line. However, wave activity is significantly diminished at the MA station. The different responses observed at the stations (totality versus partial eclipse) may possibly be attributed to the change rate of the EUV scaling factor (greater versus smaller gradient). Particularly, the sharp transition before and after totality when the signs of the change rate flip imposes a *wave-like* forcing to the atmosphere. The right panel of Figure 1 shows that the change rate changes from negative to positive as the lunar shadow comes toward and then goes away from the observer. The piecewise change rate can be linearly approximated by three straight lines, marking the middle section the *transition*. Where the transition intersects with the other two lines at either sides determines the transition duration. As at a totality location the transition takes less than 3 min, oscillations of periods of a few minutes are likely to be induced. At the partial-eclipse stations, the geometry determines the duration of the transition: a shorter (longer) period of transition and a higher (lower) slope when being closer to (farther away from) the totality path. In the case of the MA station, the transition takes about 30 min at the maximal EUV obscuration and hypothetically is likely to induce oscillations of period of tens of minutes to an hour.

Figure 3 shows the logarithmic fast Fourier transform power spectrum for each percentage-differential field shown in Figure 2. A strong wave-like component of periods of 40–50 min was observable at and above 300 km in neutral density at both stations in Figures 3a and 3c. The short-period waves with periods

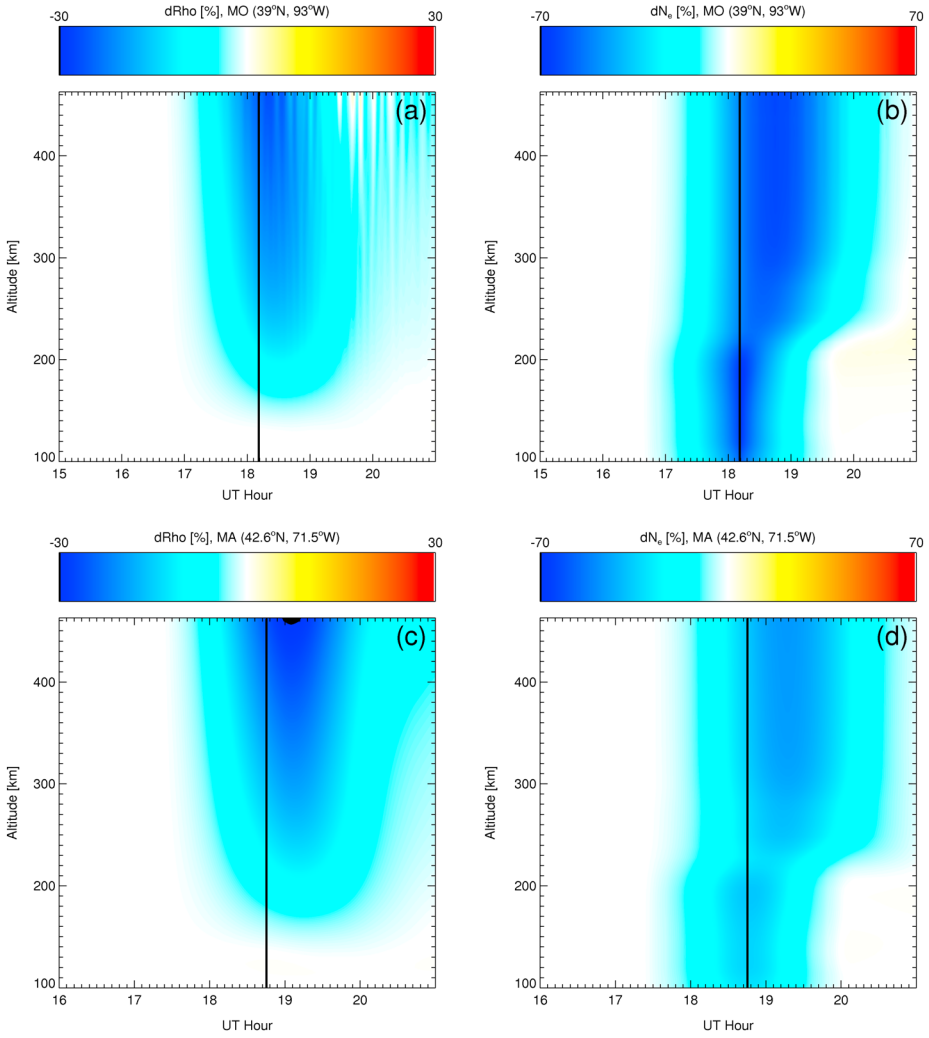

Figure 2. Differential fields of (a, c) neutral mass density and (b, d) electron density observable from the MO station undergoing totality (top row) and the MA station, where the maximal obscuration is 63% (bottom row). The maximal obscuration at each location is marked by a vertical black line.

of 5–15 min with similar strengths as the 40- to 50-min components were only observed at the totality station (MO) above 200 km but absent from the partial-eclipse station (MA). On the other hand, Figures 3b and 3d show that the waves in electron density at the totality station are strongest below 300 km. Similar to the neutral density, wave components of 5–15 min in electron density were observed only above 300 km at the MO station but less distinct at the MA station. Cautions have to be taken when interpreting the longer-period wave-like components in Figure 3. They merely represent the large-scale density depletion by the eclipse, which last about 1–2 hr as shown in Figure 2.

As waves develop in the electron density through all of the altitudes, it is expected that such wave signatures would also appear in the vertical TEC (VTEC). Electron density is height integrated up to ~450 km from the simulation results. To separate mesoscale variability from the large-scale background depletion (~ −2 TECu at maximal obscuration), a 3° zeroth-order Savitzky-Golay (Savitzky & Golay, 1964) filter of 8° in longitude/latitude was applied to the global VTEC at fixed latitudes/longitudes, respectively. Figure 4 shows the detrended results. At 18:30 UT, lunar shadow moves to around (36°N, 272°E) marked by the hollow white circle. A bow wave front had been formed by this time. As electron density grows with altitude, electron density at higher altitudes dominates the overall wave signatures observed in our results (Figure 4).

In previous studies of the lower atmosphere (Eckermann et al., 2007), weaken ozone heating was attributed to be the main source of the waves induced during a solar eclipse. One of the advantages of simulating the

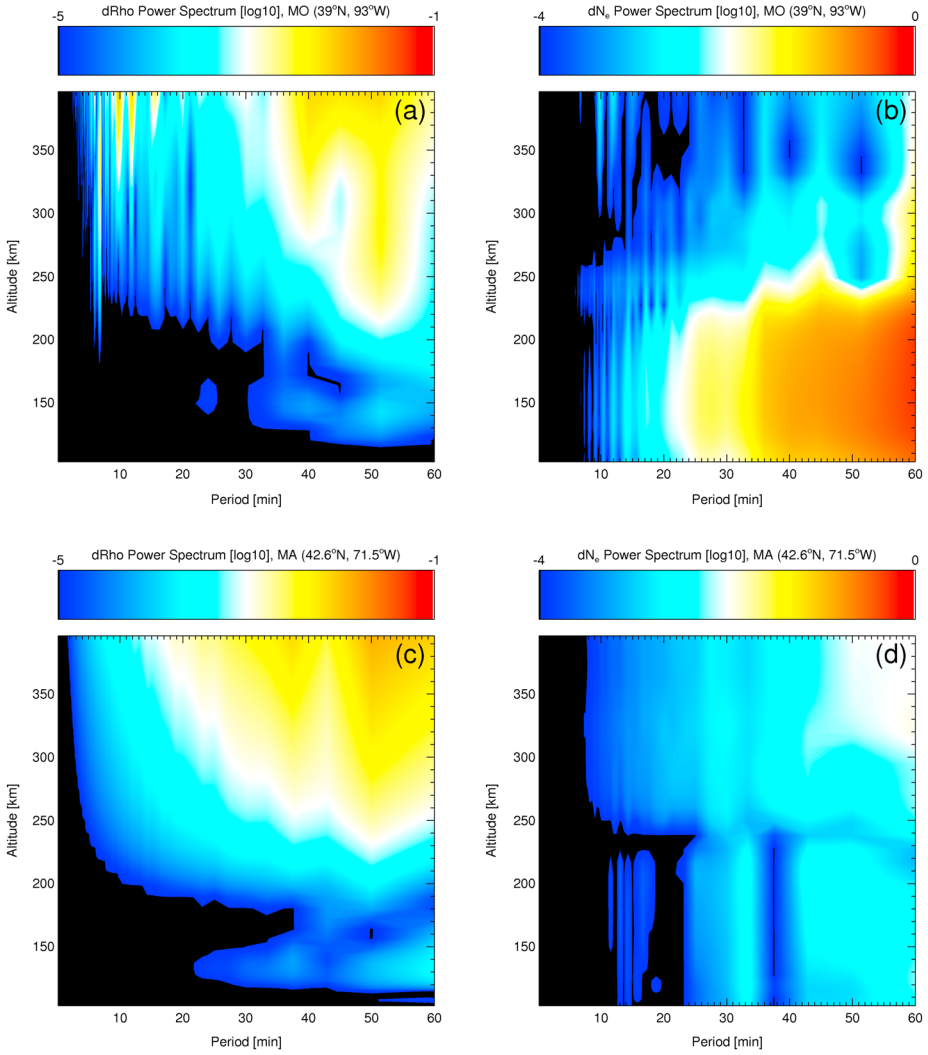

Figure 3. Periodogram of the corresponding (a, c) thermospheric and (b, d) ionospheric oscillation observable from the two stations. The panels are orientated similarly to the ones in Figure 1.

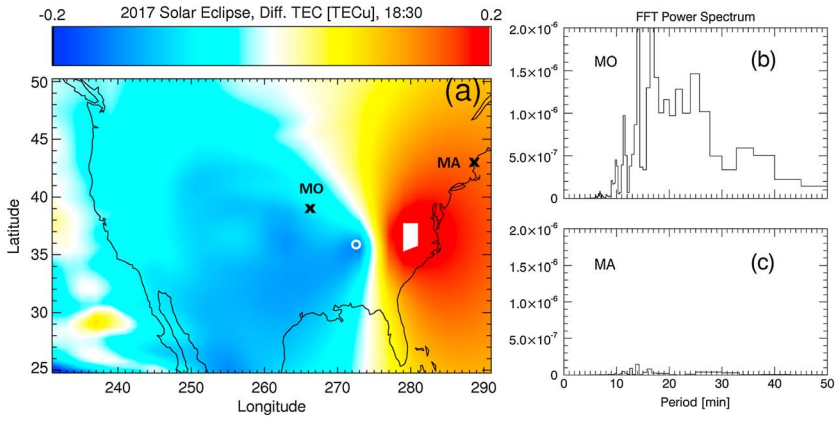

Figure 4. Detrended observable total electron content (TEC) perturbations. (a) A clear bow wave front formed as the eclipse moves across the United States and the crosses from west to east mark the (b) MO and (c) MA stations, where the fast Fourier transform (FFT) power spectra are derived from the high-cadence vertical TEC output. The lunar shadow is marked by the hollow white circle. The quadrangular white area in (a) indicates perturbation magnitude exceeding 0.2 TECu.

solar eclipse event is that it was possible to distinctly investigate if in situ forcing in the upper atmosphere contributed to the observed bow waves and gravity waves in TEC. Figure 4a shows that a bow wave front can be formed with only the in situ modification to the forcing and without a lower-atmospheric source. The bow wave front led by the lunar shadow had a magnitude of −0.2 TECu, which agrees well with the magnitude reported in Zhang et al. (2017). The quadrangular white area in Figure 4a indicates perturbation magnitude exceeding 0.2 TECu. The high-resolution and high-cadence GITM outputs also allowed the extraction of high-frequency wave components that were close to the local buoyancy frequency. From west to east, two crosses in Figure 4a mark the locations of the MO and MA stations. A 3° zeroth-order Savitzky-Golay filter of 60 min was applied to the VTEC at these locations. Figures 4b and 4c show the FFT power spectra of the detrended VTEC perturbations at the two stations. The detrended VTEC displays significant wave activity lasting at least 2 hr at the totality station since the passing of the lunar shadow. While no clear waves were detected at the MA station, wave components of periods of 10–40 min were most prominent at the MO station. Especially, the 20- to 30-min waves dominate the spectra, which agrees well with the wave periods of mesoscale gravity waves extracted from the GNSS observations during the 2017 eclipse (Zhang et al., 2017) as well as the theoretical predictions by Chimonas and Hines (1971).

The trailing gravity waves close to the MO station in Figure 4a in our simulations showed an eastward propagation speed of 155 m/s and a southward propagation speed of 200 m/s. The waves lasted at least 1 hr since the local totality. Given the grid resolutions in this simulation is roughly equivalent to a resolution of 150 km × 50 km in the U.S. sector. The resolvable horizontal wavelength in the diagonal direction is 316 km. The bow wavelengths reported by Zhang et al. (2017) is 350/270 km in the zonal/meridional direction, equivalent to a horizontal wavelength of 442 km. However, the aspect ratio of the GITM grids is different from the one employed by Zhang et al. (2017). A projection at an angle of 19.3° between the two orientations therefore needs to be considered. Potentially, the projected wavelength of 417 km from Zhang et al. (2017) should be resolvable by the current simulation setting.

The detrending processes in this study, however, were selected best applicable to the nature of the data sets of interest and do not exactly resemble the process taken by Zhang et al. (2017), in which a low-pass filter was applied to each line-of-sight TEC profile from the GNSS satellites and the residual are binned to the 2-D plane. Even so, comparing the contour in Figure 4a (the 2-D GITM results) to Figure 2 in Zhang et al. (2017) and comparing the wave characteristics to the ones reported by the group provide a sufficient evidence to conclude that bow waves of similar characteristics are reproduced in the model given the limitation of different approaches. This may not, however, conclusively show the waves presented in this work are the exactly same modes of waves as those presented in Zhang et al. (2017). Caution has to be taken when making a direct comparison between our simulation results and observations. The study by Mrak et al. (2018) has shown that the obscuration of an unevenly distributed EUV flux (two active regions present) from the solar atmosphere on 21 August 2017 might have imposed wave-like features with an amplitude of ~±0.2 TECu to the observed TEC perturbations. Nevertheless, the results in this study demonstrate that the bow waves can be triggered by a solar eclipse with uniformly distributed EUV flux across the solar disk and are likely a subset of waves observed by the GNSS network even without the inclusion of the consequential temporal evolution of the EUV flux related to its spatial distribution across the solar atmosphere.

4. Summary

In this study, GITM was used to simulate the 2017 solar eclipse event with high-resolution and high-cadence outputs. Strong high-frequency mesoscale wave activity was observable in both neutral and electron densities at the totality station but absent from the partial-eclipse station. Particularly, the high-frequency wave components (periods of <15 min) observed in neutral density were as strong as the lower-frequency components (periods of ~60 min) at the totality station. The different responses observed at the totality and partial-eclipse stations are attributed to the rate of change of the EUV scaling factor. Strong wave activity in electron density contributes to the VTEC perturbations at the totality station, with the strongest waves having periods of 20–30 min lasting at least 2 hr since totality. The detrended VTEC revealed a bow wave front led by the lunar shadow. The perturbation magnitude of −0.2 TECu associated with 20- to 30-min waves agrees well with the characteristics observed by the GNSS network. Using GITM, we were able to confirm the generation of observable bow waves and gravity waves by differential in situ heating during a solar eclipse.

Acknowledgments

This research at the University of Texas at Arlington was supported by NSF through grant ATM0955629, NASA through grants NNX13AD64G and NNX14AD46G, and AFOSR through awards FA9550-16-1-0059 and MURI FA9559-16-1-0364. The authors acknowledge the Texas Advanced Computing Center (TACC) at the University of Texas at Austin for providing Lonestar5 and Maverick resources that have contributed to the research results reported within this paper. URL: http://www.tacc.utexas.edu. The GITM model outputs are available at https://github.com/cissilin/Lin2018GRL_SolarEclipse.

References

Altadill, D., Solé, J. G., & Apostolov, E. M. (2001). Vertical structure of a gravity wave like oscillation in the ionosphere generated by the solar eclipse of August 11, 1999. *Journal of Geophysical Research*, *106*(A10), 21,419–21,428. https://doi.org/10.1029/2001JA900069

Chimonas, G. (1970). Internal gravity-wave motions induced in the Earth's atmosphere by a solar eclipse. *Journal of Geophysical Research*, *75*(28), 5545–5551. https://doi.org/10.1029/JA075i028p05545

Chimonas, G., & Hines, C. O. (1971). Atmospheric gravity waves induced by a solar eclipse, 2. *Journal of Geophysical Research*, *76*(28), 7003–7005. https://doi.org/10.1029/JA076i028p07003

Coster, A. J., Goncharenko, L., Zhang, S.-R., Erickson, P. J., Rideout, W., & Vierinen, J. (2017). GNSS observations of ionospheric variations during the 21 August 2017 solar eclipse. *Geophysical Research Letters*, *44*, 12,041–12,048. https://doi.org/10.1002/2017GL075774

Deng, Y., Richmond, A. D., Ridley, A. J., & Liu, H.-L. (2008). Assessment of the non-hydrostatic effect on the upper atmosphere using a general circulation model (GCM). *Geophysical Research Letters*, *35*, L01104. https://doi.org/10.1029/2007GL032182

Deng, Y., & Ridley, A. (2014). Simulation of non-hydrostatic gravity wave propagation in the upper atmosphere. *Annales Geophysique*, *32*(4), 443–447. https://doi.org/10.5194/angeo-32-443-2014

Eckermann, S. D., Broutman, D., Stollberg, M. T., Ma, J., McCormack, J. P., & Hogan, T. F. (2007). Atmospheric effects of the total solar eclipse of 4 December 2002 simulated with a high-altitude global model. *Journal of Geophysical Research*, *112*, D14105. https://doi.org/10.1029/2006JD007880

Fritts, D. C., & Luo, Z. (1993). Gravity wave forcing in the middle atmosphere due to reduced ozone heating during a solar eclipse. *Journal of Geophysical Research*, *98*(D2), 3011–3021. https://doi.org/10.1029/92JD02391

Galvan, D. A., Komjathy, A., Hickey, M. P., & Mannucci, A. J. (2011). The 2009 Samoa and 2010 Chile tsunamis as observed in the ionosphere using GPS total electron content. *Journal of Geophysical Research*, *116*, A06318. https://doi.org/10.1029/2010JA016204

Hickey, M. P., Schubert, G., & Walterscheid, R. L. (2009). Propagation of tsunami-driven gravity waves into the thermosphere and ionosphere. *Journal of Geophysical Research*, *114*, A08304. https://doi.org/10.1029/2009JA014105

Huba, J. D., & Drob, D. (2017). SAMI3 prediction of the impact of the 21 August 2017 total solar eclipse on the ionosphere/plasmasphere system. *Geophysical Research Letters*, *44*, 5928–5935. https://doi.org/10.1002/2017GL073549

Jakowski, N., Stankov, S. M., Wilken, V., Borries, C., Altadill, D., Chum, J., et al. (2008). Ionospheric behavior over Europe during the solar eclipse of 3 October 2005. *Journal of Atmospheric and Solar-Terrestrial Physics*, *70*(6), 836–853. https://doi.org/10.1016/j.jastp.2007.02.016

Lin, C. Y., Deng, Y., Sheng, C., & Drob, D. P. (2017). A study of the nonlinear response of the upper atmosphere to episodic and stochastic acoustic-gravity wave forcing. *Journal of Geophysical Research: Space Physics*, *122*, 1178–1198. https://doi.org/10.1002/2016JA022930

MacPherson, B., González, S. A., Sulzer, M. P., Bailey, G. J., Djuth, F., & Rodriguez, P. (2000). Measurements of the topside ionosphere over Arecibo during the total solar eclipse of February 26, 1998. *Journal of Geophysical Research*, *105*(A10), 23,055–23,067. https://doi.org/10.1029/2000JA000145

Marriott, R. T., St, D. E., John, R. M. T., & Venkateswaran, S. V. (1971). XUV image of the sun from eclipse observations of the ionospheric E-region. *Solar Physics*, *21*(2), 483–494. https://doi.org/10.1007/BF00154303

Meng, X., Komjathy, A., Verkhoglyadova, O. P., Yang, Y.-M., Deng, Y., & Mannucci, A. J. (2015). A new physics-based modeling approach for tsunami-ionosphere coupling. *Geophysical Research Letters*, *42*, 4736–4744. https://doi.org/10.1002/2015GL064610

Mrak, S., Semeter, J. L., Drob, D., & Huba, J. B. (2018). Direct EUV/X-ray modulation of the ionosphere during the August 2017 total solar eclipse. *Geophysical Research Letters*, *45*. https://doi.org/10.1029/2017GL076771

Müller-Wodarg, I. C. F., Aylward, A. D., & Lockwood, M. (1998). Effects of a mid-latitude solar eclipse on the thermosphere and ionosphere—A modelling study. *Geophysical Research Letters*, *25*(20), 3787–3790. https://doi.org/10.1029/1998GL900045

Nishioka, M., Tsugawa, T., Kubota, M., & Ishii, M. (2013). Concentric waves and short-period oscillations observed in the ionosphere after the 2013 Moore EF5 tornado. *Geophysical Research Letters*, *40*, 5581–5586. https://doi.org/10.1002/2013GL057963

Occhipinti, G., Lognonné´, P., Kherani, E. A., & He'bert, H. (2006). Three-dimensional waveform modeling of ionospheric signature induced by the 2004 Sumatra tsunami. *Geophysical Research Letters*, *33*, L20104. https://doi.org/10.1029/2006GL026865

Perwitasari, S., Sakanoi, T., Yamazaki, A., Otsuka, Y., Hozumi, Y., Akiya, Y., et al. (2015). Coordinated airglow observations between IMAP/VISI and a ground-based all-sky imager on concentric gravity wave in the mesopause. *Journal of Geophysical Research: Space Physics*, *120*, 9706–9721. https://doi.org/10.1002/2015JA021424

Ridley, A. J., Deng, Y., & Tóth, G. (2006). The global ionosphere-thermosphere model. *Journal of Atmospheric and Solar-Terrestrial Physics*, *68*(8), 839–864. https://doi.org/10.1016/j.jastp.2006.01.008

Saito, T., Ito, Y., Inazu, D., & Hino, R. (2011). Tsunami source of the 2011 Tohoku-Oki earthquake, Japan: Inversion analysis based on dispersive tsunami simulations. *Geophysical Research Letters*, *38*, L00G19. https://doi.org/10.1029/2011GL049089

Savitzky, A., & Golay, M. J. E. (1964). Smoothing and differentiation of data by simplified least squares procedures. *Analytical Chemistry*, *36*(8), 1627–1639. https://doi.org/10.1021/ac60214a047

Tsugawa, T., Saito, A., Otsuka, Y., Nishioka, M., Maruyama, T., Kato, H., et al. (2011). Ionospheric disturbances detected by GPS total electron content observation after the 2011 off the Pacific coast of Tohoku earthquake. *Earth, Planets and Space*, *63*(7), 875–879. https://doi.org/10.5047/eps.2011.06.035

Vadas, S. L., Makela, J. J., Nicolls, M. J., & Milliff, R. F. (2015). Excitation of gravity waves by ocean surface wave packets: Upward propagation and reconstruction of the thermospheric gravity wave field. *Journal of Geophysical Research: Space Physics*, *120*, 9748–9780. https://doi.org/10.1002/2015JA021430

Yue, J., Thurairajah, B., Hoffmann, L., Alexander, J., Chandran, A., Taylor, M. J., et al. (2014). Concentric gravity waves in polar mesospheric clouds from the Cloud Imaging and Particle Size experiment. *Journal of Geophysical Research: Atmospheres*, *119*, 5115–5127. https://doi.org/10.1002/2013JD021385

Zhang, S.-R., Erickson, P. J., Goncharenko, L. P., Coster, A. J., Rideout, W., & Vierinen, J. (2017). Ionospheric bow waves and perturbations induced by the 21 August 2017 solar eclipse. *Geophysical Research Letters*, *44*, 12,067–12,073. https://doi.org/10.1002/2017GL076054